Synergistic effect of single-atom Cu and hierarchical polyhedron-like Ta$_3$N$_5$/CdIn$_2$S$_4$ S-scheme heterojunction for boosting photocatalytic NH$_3$ synthesis

Zhiyuan Liu [a], Shiying Fan [a], Xinyong Li [a,*], Zhaodong Niu [a], Jing Wang [a], Chunpeng Bai [a], Jun Duan [a], Moses O. Tadé [b], Shaomin Liu [b]

[a] *State Key Laboratory of Fine Chemicals, Key Laboratory of Industrial Ecology and Environmental Engineering (MOE), School of Environmental Science and Technology, Dalian University of Technology, Dalian 116024, PR China*
[b] *Department of Chemical Engineering, Curtin University, GPO Box U1987, Perth, WA 6845, Australia*

ABSTRACT

Achieving synergy between single atomic site and charge transfer in heterojunction is significant for synthesising photocatalysts with excellent properties. In this paper, single atom Cu/Ta$_3$N$_5$/CdIn$_2$S$_4$ S-scheme hierarchical polyhedrons (SACu/TN/CIS SHPs) have been successfully synthesized by a three-step simple chemistry process. We dive into the improvement of photocatalytic activity in the synergistic effect of SACu and S-scheme. The excellent charge separation and reducing the energy barrier during the ammonium production reaction in the synergistic effect were confirmed by density functional theory (DFT) calculations and physicochemical mechanistic investigations. Electron spin resonance (ESR) corroborated production of reducing agent to accelerate the progress of NO$_3^-$ to NH$_3$. Under light conditions, the NH$_3$ production rate for SACu/TN/CIS SHPs is an astonishing ~43.6 times higher than that of original Ta$_3$N$_5$. This report not only recommends an efficient catalyst under visible light, but also proposes an advantageous solution for photocatalytic nitrate reduction in natural conditions.

1. Introduction

In recent decades, modern industrial waste disposal, the agriculture, livestock industries and other unrestrained anthropogenic activities, have led to a dramatic increase in the accumulation of nitrate [1,2]. It is worth noting that in the human digestive system, the reduction of nitrates, which are relatively non-toxic in themselves, to toxic nitrites by microorganisms is readily achieved. The direct or indirect ingestion of water and plants containing nitrates is a threat to human health [3–5]. The National Academy of Engineering considers the effective treatment of nitrate in water to be the major and urgent challenge of the century in view of these harmful effects on human health [6]. Among nitrate treatment methods, denitrification is the conversion of nitrate into N$_2$ and can be achieved by the anaerobic bacteria and physicochemical method. The conversion of nitrate to ammonia is of greater application from both an environmental and renewable energy perspective [7]. The core of the problem of nitrate conversion from water has always been its own stability and selectivity properties. Many biological, chemical and physical techniques (such as ion exchange and photo(electro)catalysis) have been used to transform NO$_3^-$ in liquid phase, especially significant efforts have recently focused on selective heterojunction catalysts for the ammonium production route with the removal of NO$_3^-$ [8–12]. The intrinsically weak NO$_3^-$ removal and poor ammonium selectivity can lead to increased underutilization of energy. During the catalytic conversion process, byproducts such as nitrite (NO$_2^-$) might be generated. A satisfied conversion of NO$_3^-$ to NH$_4^+$ is required with fewer or no unwanted byproducts in the reaction [13–20]. Hence, tremendous efforts, including regulation of unique active interfaces, adsorption of nitrate by functional groups and aromatic structures, and reduction of reaction energy barriers by metal co-catalyst, have been devoted to solving these issues [10–12]. Among the heterogeneous catalysts, photocatalysts containing metal co-catalysts show promising ammonium generation rates for the under mild conditions.

Ta$_3$N$_5$ is considered as a favorable competitor for its simple chemical composition and band gap energy of ~2.0 eV in visible light energy conversion. This material has been reported as early as 2002 due to its

---

* Corresponding author.
E-mail address: xyli@dlut.edu.cn (X. Li).

simultaneous H^+ reduction and H_2O oxidation band structure. Since then, various methods have been utilized to achieve breakthroughs in the visible light conversion field of Ta_3N_5, including morphology control and element doping [21–28]. In addition, exhilarating development have been made in structural optimization, such as S-scheme photoelectrochemical energy conversion [29–33]. Although many efforts are worthy of recognition, selective conversion of nitrate is not yet satisfactory on the Ta_3N_5 for its charge recombination and lack of active site. Therefore, the challenge remains to optimize and improve Ta_3N_5 for the specific conversion of NO_3^- to NH_3 under visible light [34,35].

A prerequisite for metal compounds to be deposited on the surface in the desired manner is the availability of a suitable catalyst carrier and reaction control to the extent that nanocomposite particles are formed on the carrier surface that can be used as active sites, ultimately leading to the modification of the interfacial structure. The construction of interfacial structures and active sites should focus on promoting ammonia production and inhibiting side reactions to improve efficiency, and meet the challenges in uncovering the mechanisms that influence activity in the construction. The potential visible catalyst $CdIn_2S_4$ has be found in numerous studies on photoactivated radicals and degradation of hazardous organic pollutants, which are known for their stability and have attracted considerable attention [36–40]. From previous studies, it can be concluded that the microstructure largely determines the catalytic activity of $CdIn_2S_4$ [36,38]. Among the many favored morphologies of co-catalysts, $CdIn_2S_4$ nanoparticles have unique advantages in terms of specific surface area and quantum confinement effects with its own nanometer dimensions [39]. These phenomena provide inspiration to construct a $Cu/Ta_3N_5/CdIn_2S_4$ composite for rationalizing the activity and selectivity of direct photoreduction of NO_3^- to NH_3 in the perspective of nano-studies.

In this work, a single-atom-containing S-scheme photocatalyst is proposed for highly selective conversion of NO_3^- to NH_3. The photocatalyst is a Ta_3N_5-based composite material ($Cu/Ta_3N_5/CdIn_2S_4$ S-scheme hierarchical polyhedrons (SACu/TN/CIS SHPs)) on which SACu sites and CIS nanoparticles are composited together. The synergic effect or action among three components in the SACu/TN/CIS SHPs enables the specific conversion of NO_3^- to NH_3. We found that the excellent charge separation of S-scheme of TN and CIS continuously provides effective energy for the entire reaction. At the same time, SACu, as the main active site, effectively reduces the energy barriers during the transformation. The CIS promotes the generation of in situ $\cdot CO_2^-$ through formic acid splitting, which immediately participates in the progress as a reductant of NO_3^- to NH_3 under irradiation. The synergic mechanism and charge transfer process are testified in detail.

2. Experimental section

2.1. Synthesis of Ta_3N_5 hierarchical polyhedrons (TN HPs)

Firstly, we prepared Ta_xO_y by a wet impregnation method. 100 ml $TaCl_5$ alcoholic solution was treated with a 70 °C water bath for 12 h. Then, Ta_xO_y was obtained by purification prior to drying at 100 °C for 2 h. The thermal nitridation process of Ta_xO_y was carried out in a vacuum tube furnace [41]. 2.0 g Ta_xO_y and 5.0 g melamine were arranged in a vacuum tube furnace at 700 °C for 6 h. Finally, TN HPs were collected.

2.2. Synthesis of Cu single atoms dispersed Ta_3N_5 hierarchical polyhedrons (SACu/TN HPs)

A corresponding mass ratio of Cu/Ta_3N_5 hierarchical polyhedrons were obtained by adding required amounts of $Cu(NO_3)_2 \cdot 6H_2O$ aqueous solution into TN HPs. A well-stirred mixture needs to be dried at 80 °C for 24 h, and then calcined at 400 °C in 5 % hydrogen atmosphere [42]. The $Cu/CdIn_2S_4$ was also prepared, except that TN HPs were replaced by $CdIn_2S_4$.

2.3. Synthesis of single atoms $Cu/Ta_3N_5/CdIn_2S_4$ S-scheme hierarchical polyhedrons (SACu/TN/CIS SHPs)

Add a corresponding mass ratio of SACu/TN to the 30 ml of chloride (1.0 mmol) and indium chloride (2 mmol) solution that had been stirred and continue stirring for one hour. Thiourea aqueous solution (5 mmol in 25 ml) was slowly dripped into mixed solution, and stirred for another 1 h. The well-stirred mixed solution was kept in a 200 ml teflon-lined autoclave at 200 °C for 15 h [43]. The solid composite was filtrated by centrifugation and wash with deionized water and ethanol, and dried in 80 °C vacuum environment for 24 h. Simultaneously, for further comparison, the pure $CdIn_2S_4$ was also prepared. The $Ta_3N_5/CdIn_2S_4$ hierarchical polyhedrons were prepared without containing Cu.

2.4. The photocatalytic conversion evaluation

Photoreduction nitrate tests were achieved in a 250 ml hermetic quartz reactor vessel with a 250 W Xenon lamp. Constant flow of water controlled the solution temperature at 25 °C. 50 mg of the catalyst and 10 ml FA were dispersed into 75 ml nitrate solution (0.4 mmol L^{-1}). Before turning on the Xenon lamp, the mixed suspension needed to be treated with inert gas for 30 min. During the 2 h reaction time, the suspension was extracted at regular intervals, and immediately extracted through 0.22 μm cellulose acetate membrane. The contents of NO_3^- and NO_2^- were quantified by an ICS-90A ion chromatography. The content of NH_4^+ in the solution was determined by the standard Nessler's reagent colorimetric method. N_2 was determined by a gas chromatography. The main products of nitrate photoreduction include NO_2^-, NH_4^+ and N_2 [44]. The NO_3^- remove and NH_4^+ selectivity are calculated from Eqs. (1) and (2), respectively.

$$\eta_{NO_3^-} = \left(1 \cdot \frac{(NO_3^-)_0 - (NO_3^-)_t}{(NO_3^-)_0} \right) \times 100\% \tag{1}$$

$$S_{NH_4^+} = \left(1 \cdot \frac{(NO_3^-)_0 - (NO_3^-)_t - (NO_2^-)_t - (N_2)_t}{(NO_3^-)_0 - (NO_3^-)_t} \right) \times 100\% \tag{2}$$

Where (nitrogen species)$_{0/t}$ (mmol·L^{-1}) represent the concentration at time.

3. Results and discussion

3.1. Morphology and microstructure analysis

TN HPs were firstly prepared by thermal nitridation of amorphous tantalum oxide[45]. SACu/TN HPs with weight ratio of 1:69 were fabricated by a simple wet impregnation method (Fig. 1a). The X-ray diffraction (XRD) pattern (Fig. 1b) of the SACu/TN HPs points out that all the peaks are attributed to the Cu (JCPDS no. 04–0836) and Ta_3N_5 (JCPDS no. 89–5200) phases. The scanning electron microscope (SEM) images illustrate that the TN and SACu/TN exhibit an irregular hierarchical polyhedrons structure with a size of ~300 nm (Fig. S1a and b). Then, CIS nanoparticles with an amount of 30.00 wt% were deposited on the SACu/TN HPs by hydrothermal method (Fig. 1c). The obtained sample was denoted as SACu/TN/CIS SHPs. Discernible XRD diffraction pattern of the $CdIn_2S_4$ (JCPDS no. 27–0060) was described, due to the high crystallinity and dispersion of CIS on the SACu/TN/CIS SHPs. The existing content of Cu and CIS detected by inductively coupled plasma-optical emission spectroscopy is 0.98 % and 30.56 wt%, respectively (Table. S1). As demonstrated in the scanning transmission electron microscopy (STEM) images (Fig. 1d and e), the CIS nanoparticles and SACu are randomly dispersed on the SACu/TN/CIS SHPs, and the particle dimension of CIS nanoparticles is somewhere between 10 and 15 nm. The HAADF-STEM image (Fig. 1f) shows that the lattice spacings of 0.36 and 0.32 nm corresponded to Ta_3N_5 (1 1 0) and $CdIn_2S_4$
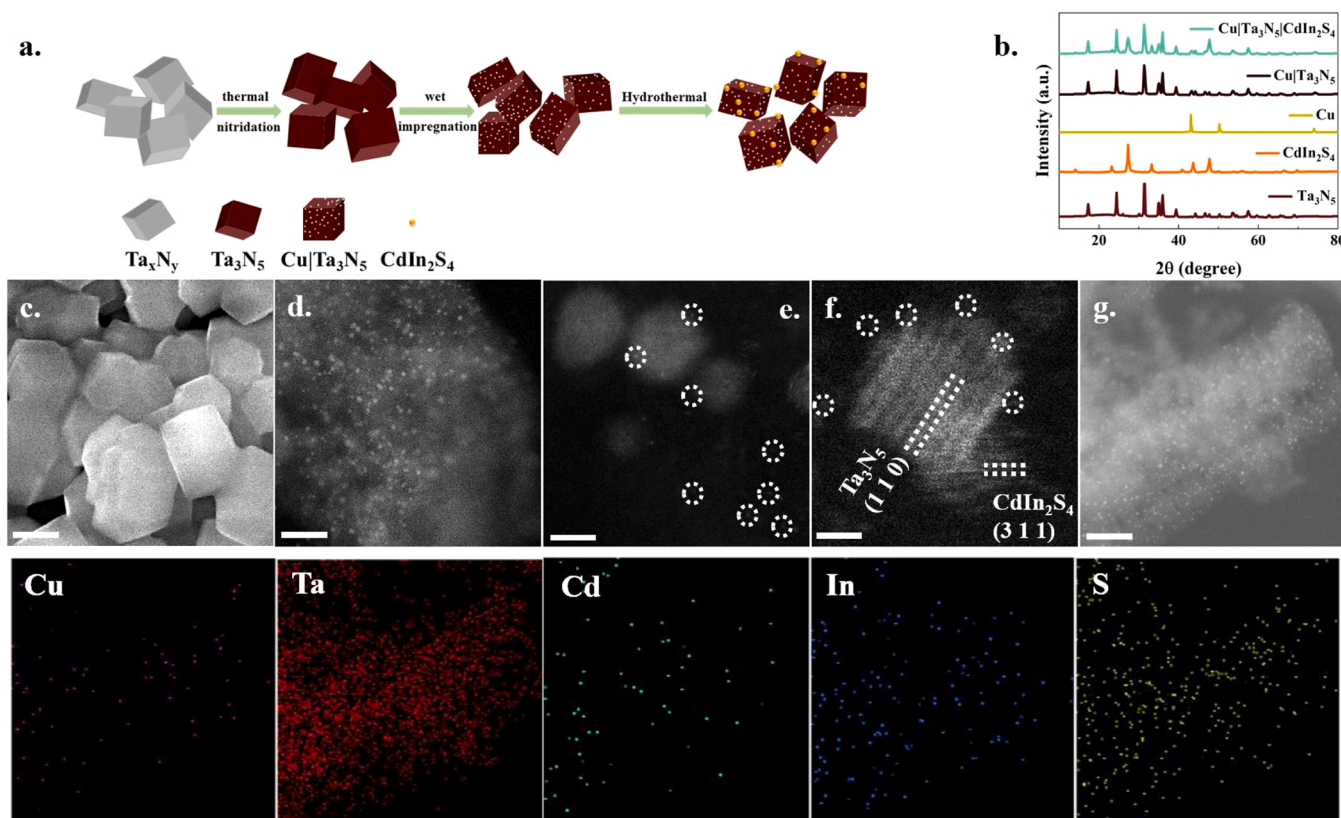
Fig. 1. (a) The preparation process of SACu/TN/CIS SHPs; b. the XRD measurements; c. the SEM image of SACu/TN/CIS SHPs (The ruler is 300 nm); d-f. the STEM images of CIS and Cu regions from SACu/TN/CIS SHPs (The rulers are 100 nm, 10 nm and 2 nm); g. the STEM elemental mapping images of SACu/TN/CIS SHPs (The rulers are 200 nm).

(3 1 1) planes, respectively. The distinct interfaces among SACu, TN and CIS can be recognized in the SACu/TN/CIS SHPs. The STEM energy-dispersive X-ray elemental mapping images (Fig. 1g) reveal that Cu, Ta, Cd, In and S are homogeneously distributed over the SACu/TN/CIS SHPs.

### 3.2. Surface chemical state analysis

The chemical states of prepared materials were further detected by X-ray photoelectron spectroscopy (XPS). The existences of Cu, Ta, N, Cd, In and S in the SACu/TN/CIS SHPs were as exhibited by the XPS patterns (Fig. 2 and S2). The symmetrical Ta 4f doublets of Ta^{5+} ions appear in the ex-situ Ta 4f XPS patterns of TN, TN/CIS and SACu/TN/CIS SHPs (Fig. 2a). The N 1s peaks at 396.6 and 403.7 eV in Fig. S2a are assigned to N^{3-} and free nitrogen. The Cd 3d, In 3d and S 2p binding energy of CdIn$_2$S$_4$ were 404.8, 411.6, 444.3, 451.8, 161.2 and 162.5 eV (Fig. 2c, d and S2b). Obviously, the binding energy of Ta 4f and N 1s in the TN/CIS and SACu/TN/CIS SHPs appeared to move 0.16 eV toward a lower binding energy as compared with the TN, while the Cd 3d, In 3d and S 2p binding energy of the TN/CIS and SACu/TN/CIS SHPs became more positive in comparison with the CIS. The difference of their work functions dominates that the electrons transferring from TN to CIS upon hybridization[46]. An IEF (internal electric field) between interfaces pointing from TN to CIS was established by the electrons transferring. The IEF is favourable bedrock for the S-scheme construction of TN/CIS without any adscititious mediator, which would efficiently prevent charge recombination and thus accelerate the NO$_3^-$ photoreduction. The main salient points appear at 932.0 and 952.8 eV positions in Cu 2p pattern (Fig. 2b). And Cu LMM Auger (Fig. S2c) were attributed to the Cu monovalent [47]. The SACu electronic structure based on SACu/TN/CIS SHPs' own proprietary was authenticated by XAFS.

Compared with metallic Cu, the presence of SACu in the SACu/TN/CIS SHPs is shown between the white lines of higher energy Cu K-edge of Cu$_2$O and CuO (Fig. 2e). The SACu positive oxidation state in the SACu/TN/CIS SHPs caused by the transfer of partial electron to its co-ordinated atoms is confirmed by the relative position mentioned above. In the Fourier transformed EXAFS pattern (Fig. 2f), the dominant peak of SACu/TN/CIS SHPs locates at 1.51 Å belonging to the Cu–N bond in the R space. Simultaneously, recognizable peaks attached to the Cu–Cu for metallic Cu at 2.20 Å and Cu–O for Cu$_2$O at 1.40 Å can't be detected, testifying that the Cu atoms are atomically distributed and corresponding to the HAADF-STEM summary. We had further revealed the coordination environment of SACu by numerical fitting in Fig. 2g. According to the EXAFS fitting, the SACu on SACu/TN/CIS SHPs is coordinated with six N atoms in the form of Cu–N$_6$ (Table. S3).

3.3. Optical and photoelectrochemical properties

The calculated electrostatic potentials show that the work functions of CdIn$_2$S$_4$ (2 2 0) and Ta$_3$N$_5$ (1 1 0) are 6.38 and 4.35 eV, respectively (Fig. 3a and b). Hence, the TN's Fermi level is higher than the CIS. Electrons spontaneously transferred from TN to CIS between the same Fermi levels when TN and CIS were connected, which led to the IEF formation at TN/CIS interfaces [48]. Besides, the calculated PDOS show that the CB (conduction band) and VB (valence band) edges of CdIn$_2$S$_4$ (2 2 0) consist of In 5 s and S 3p states, respectively, while the CB and VB edges of Ta$_3$N$_5$ (1 1 0) consist of Ta 5d and N 2p states, respectively (Fig. 3c and d). Hence, in the S-scheme process, the Ta 5d and S 3p states are the main reducing and oxidizing centers. These results were a further affirmation of the above XPS results. The establishment of the S-scheme is the basis for guaranteeing the charge separation and NO$_3^-$ photoreduction activity.
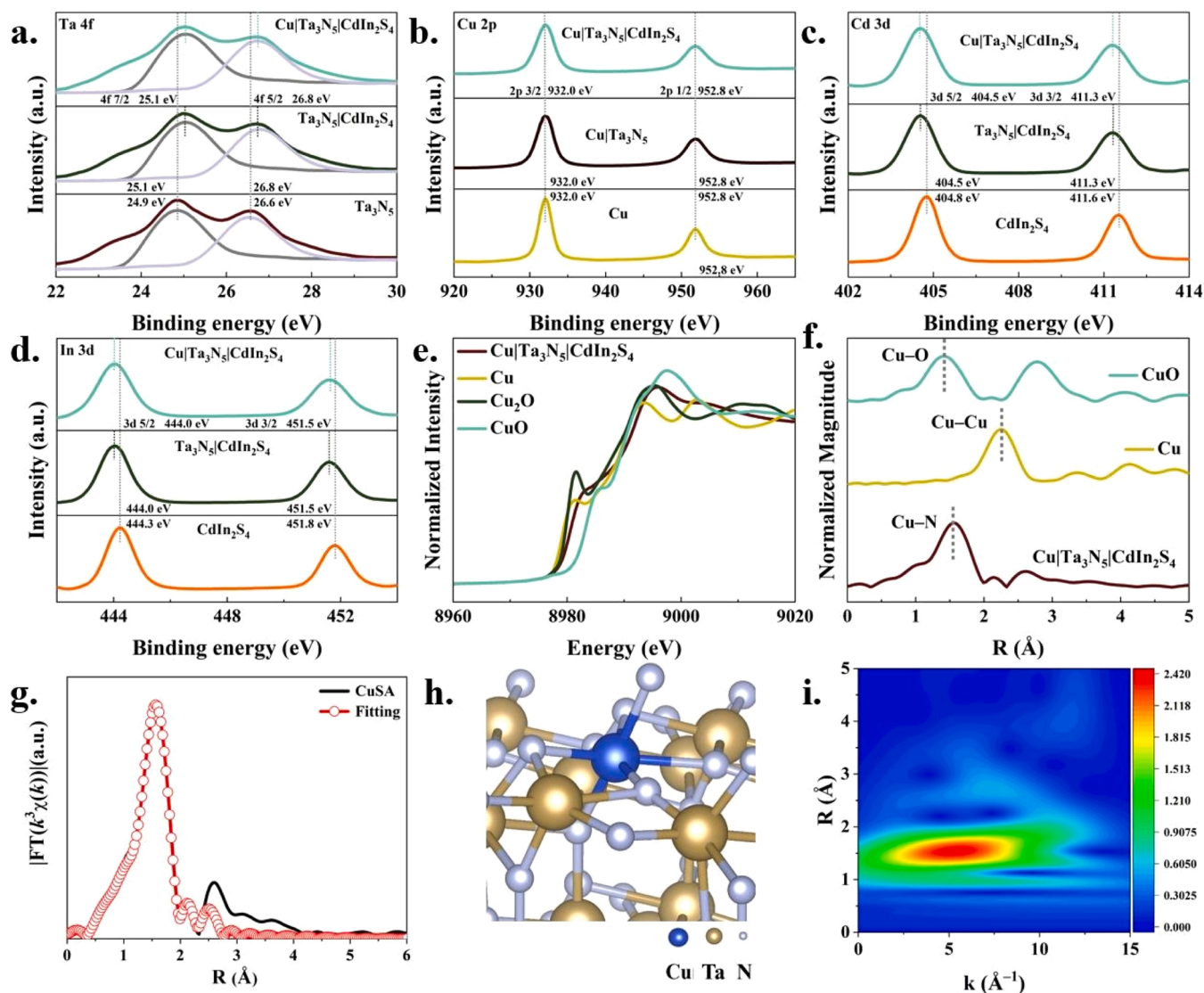
Fig. 2. (a–d.) XPS spectra of a Ta 4f, Cu 2p, Cd 3d and In 3d; e. normalized Cu K-edge XANES spectra; f. fourier transform of EXAFS for SACu/TN/CIS SHPs and references; g. EXAFS fitting result of SACu on SACu/TN/CIS SHPs; h. coordination structure of SACu on SACu/TN/CIS SHPs; i. wavelet transform analysis from EXAFS of SACu on SACu/TN/CIS SHPs.

The UV–vis (UV–vis diffuse reflectance spectrometer) was to probe the ability of catalysts in terms of optical absorption (Fig. 3e and f). The absorption edges of TN and CIS were detected at 635 and 563 nm, conforming to the band gap of 1.95 and 2.20 eV. In comparison with pristine TN, the TN/CIS and SACu/TN/CIS SHPs exhibited mildly ameliorated absorbance around visible light range.

3.4. Photocatalytic activity tests

To appraise the photocatalytic reduction capacity of SACu/TN/CIS SHPs, the nitrate removal and conversion to NH_3 was compared among the bare TN, CIS, SACu/TN, TN/CIS and SACu/TN/CIS SHPs (Fig. 4a). Only NH_3 with low selectivity was produced over the TN/CIS, indicating undesirable photocatalytic efficiency. The catalytic activity was significantly improved after SACu loading. Here, the SACu/TN/CIS SHPs led to a considerable improvement in NH_3 production with high selectivity. The yield of NH_3 reached 256.3 $\mu mol \ g^{-1} \ h^{-1}$ and the selectivity was satisfactorily mentioned as 88.7 %. The photoreduction activities continuously increased with SACu loading from 0.1 to 1.0 wt% (Fig. 4b). However, the conversion tended to stabilize while the selectivity decreased slightly with increasing SACu loading to 1.2 wt%. It was show

that the SACu loading amount of 1.0 wt% was the propitious amount for the reaction. The results confirmed that SACu was the main active site that guaranteed satisfied reduction activity for NO_3^- to NH_3, rather than semiconductors. The dark control group confirmed that the SACu/TN/CIS SHPs was catalytically inactive in the absence of sunlight, signifying that effect of SACu/TN/CIS SHPs for the overall reaction can be ignored in the dark (Table. S2).

The activities of SACu/TN/CIS SHPs with different CIS weight content were researched. The NH_3 production increases intermittently and then decreases with the loading amount of CIS in Fig. 4c. And, all SACu/TN/CIS SHPs with different CIS weight content ratios were more active than the control groups without heterojunction. The improvement of the S-scheme to the activities were mainly due to the advancement of the charge separation efficiency. The activities of SACu/TN (Fig. 4a) and SACu/CIS (Fig. 4d) are much lower than that of the SACu/TN/CIS SHPs, proving that the influence of S-scheme for increasing photocatalytic activity is critical. When CIS accounts for 30 % of the SACu/TN/CIS SHPs, the catalytic activity reaches the highest, which is the most favorable ratio for NO_3^- photoreduction.
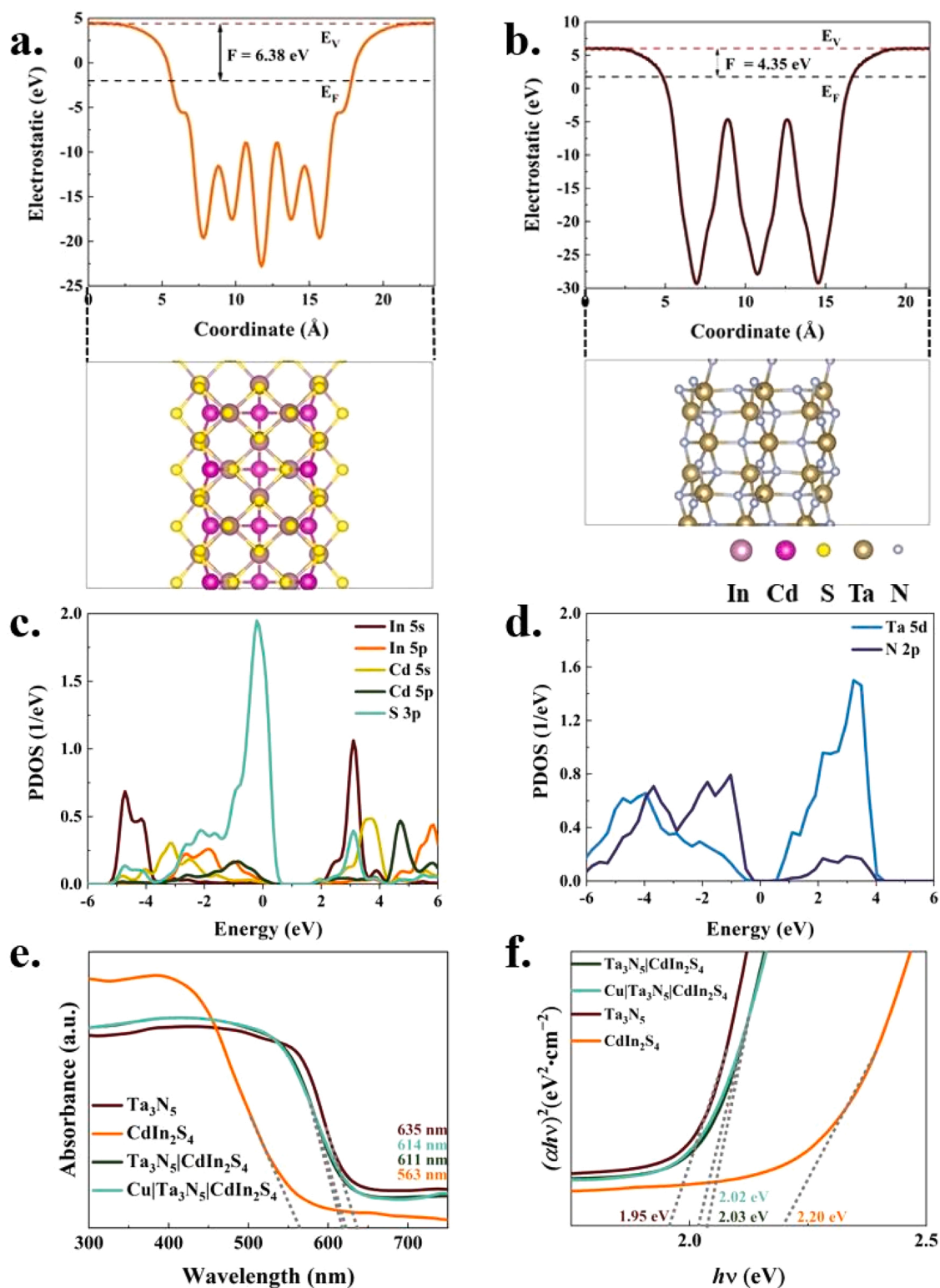
Fig. 3. a and b. The electrostatic potentials of CdIn$_2$S$_4$ (220) and Ta$_3$N$_5$ (110) facets. Black and red dashed lines indicate the Fermi and vacuum energy levels; c and d. PDOS of CdIn$_2$S$_4$ (220) and Ta$_3$N$_5$ (110) facets; e. UV–vis measurements. f. the Kubelka-Munk energy curve plots.

3.5. Mechanism investigations

The reaction mechanism of photocatalytic NO$_3^-$ was explored to enhance the comprehension for the high activity over the SACu/TN/CIS SHPs. Compared with a single semiconductor, the photocurrent densities are significantly improved due to the existence of the S-scheme (Fig. 5a). That is to say, there is a stronger photo-generated charge separation and transfer efficiency in the S-scheme. Stronger charge separation and transfer efficiency mean more photogenerated electrons and holes participating in the reaction, which is beneficial to increase the photocatalytic NH$_3$ production.

Through the detection of photoluminescence (PL) emission spectra to the samples, we have an extra understanding of the charge separation behavior in the S-scheme (Fig. 5b). For the TN/CIS, the existence of CIS
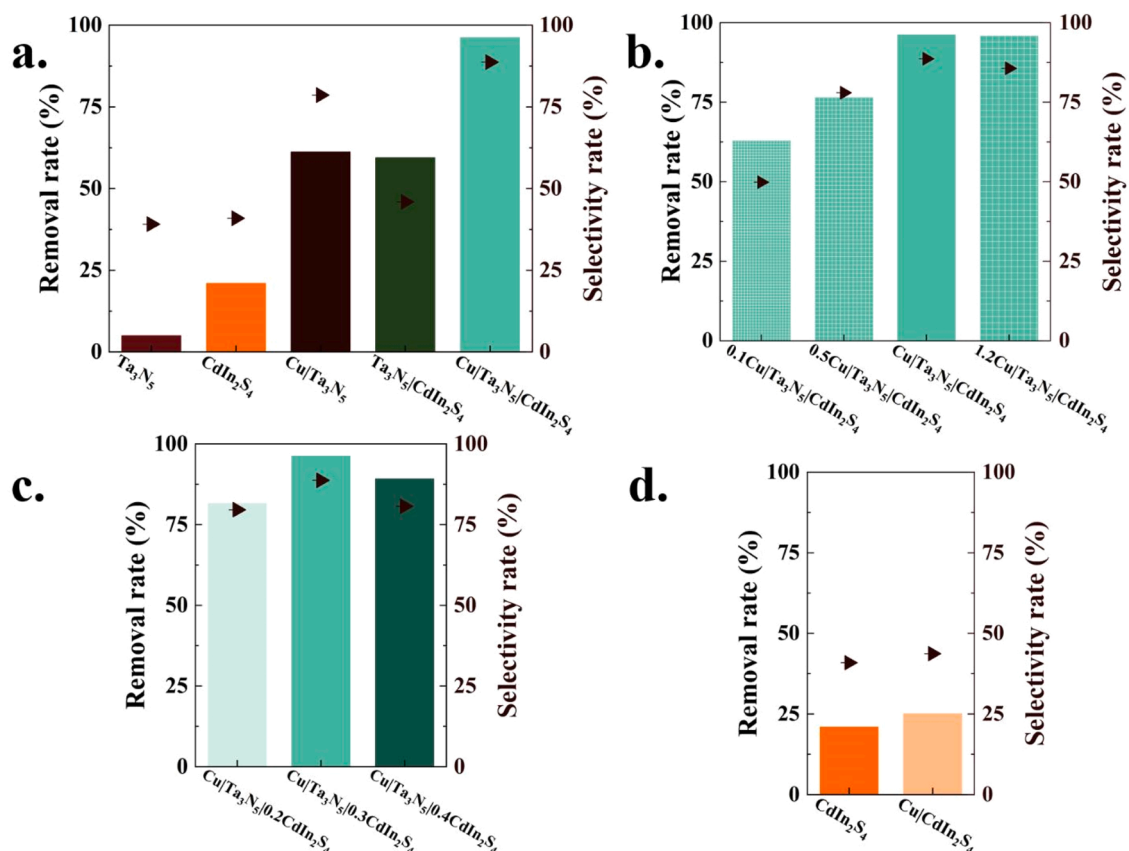
Fig. 4. (a–d.) The NO_3^- removal and selectivity measurements to NH_3.
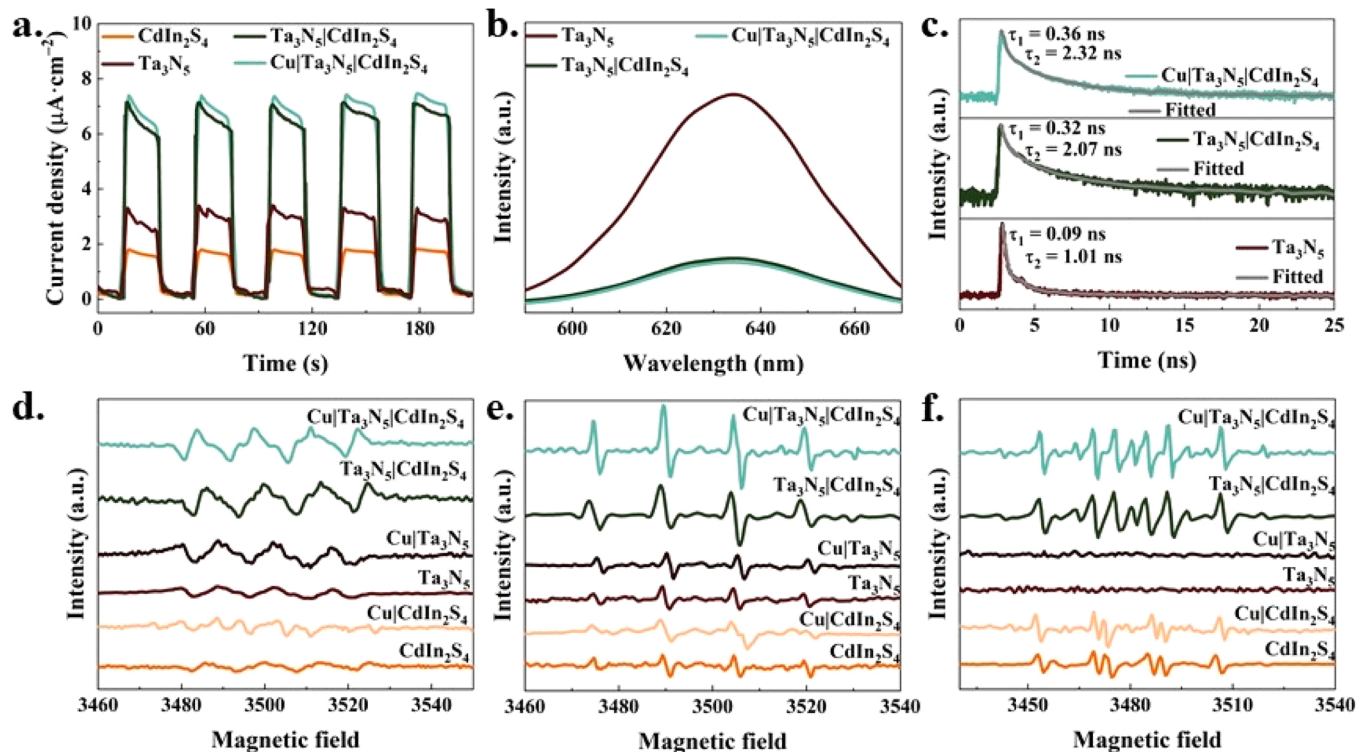
Fig. 5. (a.) The photocurrent measurements; b. photoluminescence measurements; c. time-resolved photoluminescence measurements; d-f. electron spin resonance experiments of $\cdot O_2^-$, $\cdot OH$ and $\cdot CO_2^-$.

was the main reason that directly led to the significant decrease of PL intensity than that TN. Combined with the above results of photocurrent density, the presence of CIS generated the retardation of charge recombination. Based on the detection of time-resolved PL (TRPL) spectra, we deduced the charge transfer dynamics. The lifetime (τ) of charge carriers were deduced by the decay curves. As shown in Fig. 5c, the TN/CIS has a longer τ than pristine TN, attributing the delayed recombination to the construction of S-scheme in the existence of CIS. Efficient separation of photogenerated charges is the cornerstone to ensure photocatalytic efficiency, including photocatalytic NO_3^- reduction.

When comparing the catalytic activities of various materials, we find an interesting phenomenon that the activities of bare CIS and SACu/CIS are almost the same (Fig. 4d). Compared with CIS and SACu/CIS, TN with and without Cu catalytic sites exhibited completely different catalytic activities. Not only in the control group of TN and SACu/TN, but also in the control group of TN/CIS and SACu/TN/CIS SHPs, the importance of Cu catalytic sites was clearly shown, but why did CIS and SACu/CIS exhibit the different catalytic activities? Compared with the lower CB of TN in S-scheme, the contribution of CIS to NO_3^- reduction was mainly concentrated in the VB. The VB usually participates in the reduction reaction by generating strongly reducing free radicals, so we speculate that the CIS affects the conversion of formic acid, thereby promoting the conversion efficiency of NO_3^-.

First of all, in the control group where formic acid was removed, we got preliminary confirmation. The removal of formic acid simultaneously made CIS and SACu/CIS inactive at the same time (Fig. S2d). The photogenerated holes were prone to generate $\cdot CO_2^-$, which contributed to nitrate reduction, from FA adsorbed on the catalyst surface. The in-situ electron spin resonance (ESR) experiments were explored to determine the $\cdot CO_2^-$ activation and the effect of $\cdot CO_2^-$

activation in the photocatalytic NO_3^- reduction, understanding further reaction mechanism (Fig. 5f). The results that the same $\cdot CO_2^-$ peak intensity of the CIS and SACu/CIS control groups further confirmed our conjecture. At the same time, due to the existence of the S-scheme, the charge separation efficiency was enhanced, so that the peak value of $\cdot CO_2^-$ was further improved. The VB of CIS was higher than that of TN, so in the S-scheme, the role of CIS was mainly to improve the conversion efficiency of NO_3^- by promoting the process of FA to $\cdot CO_2^-$.

The density functional theory (DFT) calculation on the SACu/TN/CIS SHPs was utilized to scrutinize the possible reaction pathways for NO_3^- reduction from a molecular perspective. The SACu/TN performs a visibly enganced photoreduction for NO_3^- to NH_3 (Fig. 6a). The calculated free energy profiles of reducing NO_3^- into NH_3 showed that the Cu surface owned a lower energy barrier (0.38 eV) for the reduction of NO_3^- than pristine Ta_3N_5 (1 1 0) surface (0.86 eV). This pointed out that the append of SACu can desirably reform the photoactivity of TN/CIS.

The underlying reaction mechanism for selective photoreduction of NO_3^- to NH_3 was proposed from the discussion of the above results, as illustrated in Eqs.3–12[49–53]. The proper bandgap structures of TN and CIS ensure the efficient establishment of S-scheme (Fig. 7). Under the illumination of light, the built-in electric field of S-scheme causes the charge to continuously separate (Eq. (3)). The electrons of TN separated by the built-in electric field can then transfer to SACu. The excellent photoreduction reaction of NO_3^- to NH_4^+ is mainly completed on SACu (Eq. (4)). Meanwhile, the holes photogenerated from CIS facilitate the FA conversion on the surface of CIS, producing the $\cdot CO_2^-$ species, which could promote NH_3 production (Eq. (7)). Compared with one-component single TN or SACu/TN, the CIS further enhances the performance of photoreduction by activating $\cdot CO_2^-$ (Eqs. (8) and (9)). Therefore, the SACu/TN/CIS SHPs is a synergistic catalyst for NH_3 production photocatalytic NO_3^- reduction with FA.

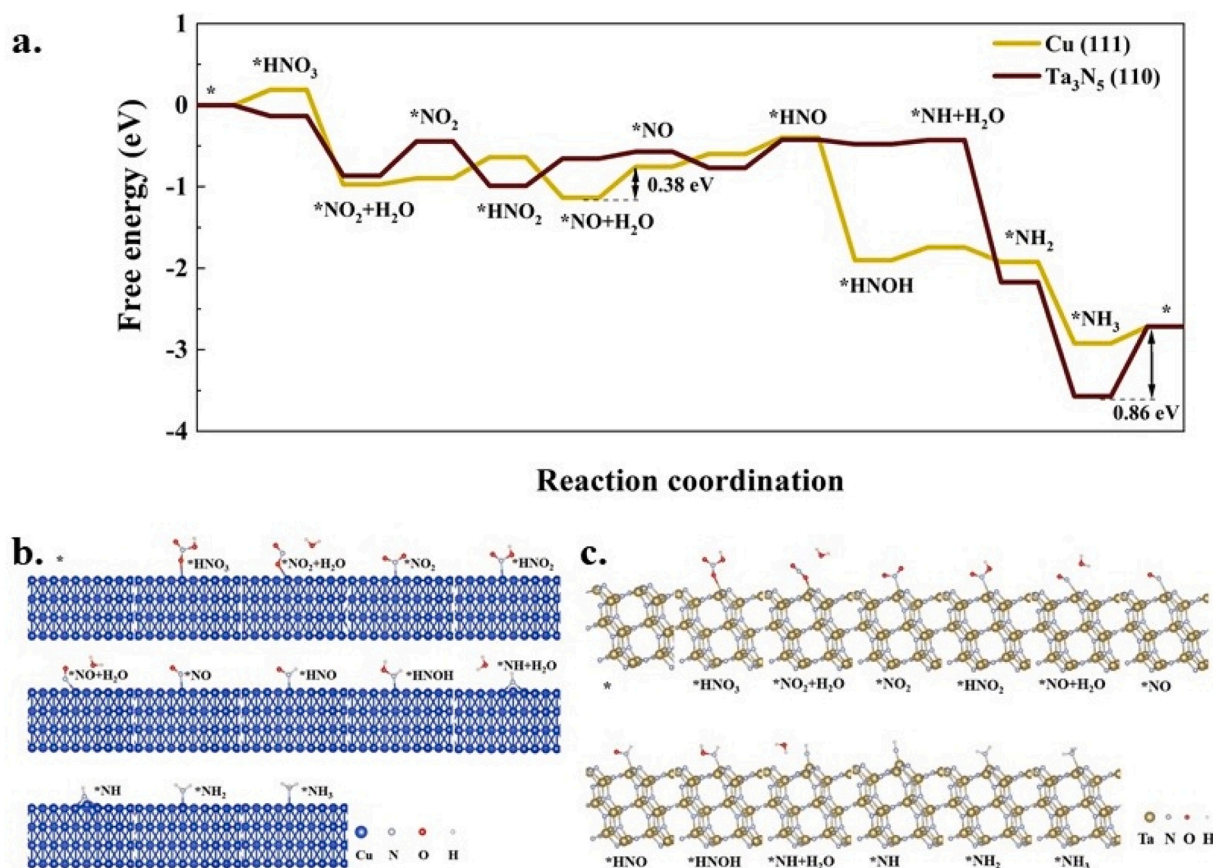**Fig. 6.** (a.) The free energy profiles of reducing NO_3^- into NH_3 on Cu (111) and Ta_3N_5 (110) surfaces; e and f. whole reaction process on Cu and Ta_3N_5.
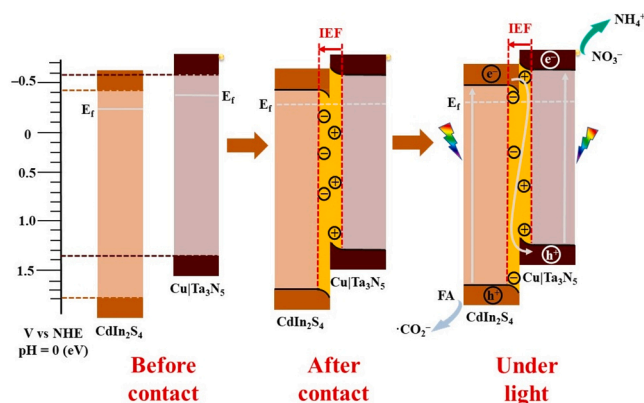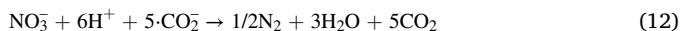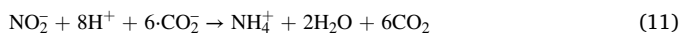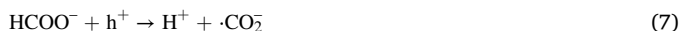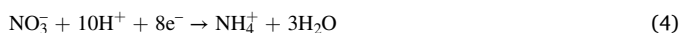
Fig. 7. S-scheme illustration of formation and charge transfer between SACu/TN and CIS for NO_3^- photoreduction.

$$Cu|Ta_3N_5|CdIn_2S_4 + h\nu \rightarrow h^+ + e^- \tag{3}$$

$$NO_3^- + 10H^+ + 8e^- \rightarrow NH_4^+ + 3H_2O \tag{4}$$

$$NO_3^- + 6H^+ + 5e^- \rightarrow 1/2N_2 + 3H_2O \tag{5}$$

$$NO_3^- + 2H^+ + 2e^- \rightarrow NO_2^- + H_2O \tag{6}$$

$$HCOO^- + h^+ \rightarrow H^+ + \cdot CO_2^- \tag{7}$$

$$H_2O + h^+ \rightarrow H^+ + \cdot OH \tag{8}$$

$$\cdot OH + HCOO^- \rightarrow \cdot CO_2^- + H_2O \tag{9}$$

$$NO_3^- + 10H^+ + 8\cdot CO_2^- \rightarrow NH_4^+ + 3H_2O + 8CO_2 \tag{10}$$

$$NO_2^- + 8H^+ + 6\cdot CO_2^- \rightarrow NH_4^+ + 2H_2O + 6CO_2 \tag{11}$$

$$NO_3^- + 6H^+ + 5\cdot CO_2^- \rightarrow 1/2N_2 + 3H_2O + 5CO_2 \tag{12}$$

The recycling photoactivities of SACu/TN/CIS SHPs for NO_3^- to NH_3 are also illustrated in Fig. S3a. After third cycles, the photocatalytic production rate of NH_3 blighted in the fourth cycle. The stability of SACu/TN/CIS SHPs was evaluate by XRD and XPS through analyzing the structure change of SACu/TN/CIS SHPs before and after photocatalytic reaction (Fig. S3b-f) [54–58]. No significant change for the SACu/TN/CIS SHPs was distinguishable in XRD pattern after photoexcitation. In XPS results, the peaks for Ta 4f, Cd 3d, In 3d and Cu 2p were still detected for the SACu/TN/CIS SHPs after cyclic reaction. Strikingly, the peaks of Cu 2p that assigned to SACu/TN/CIS SHPs decreased comparing with the that didn't participate in the reaction [59–61]. The above results revealed that, the strong redox ability of TN/CIS can only cause part of SACu to be degraded, while the remaining part of SACu on the surface of TN/CIS still played a role in the reaction.

4. Conclusions

In summary, nitrate can be efficiently and selectively photoreduced to ammonia by our prepared SACu/TN/CIS SHPs in the presence of formic acid. Our comprehensive exploration declared that the synergy between S-scheme and SACu, and activation of $\cdot CO_2^-$ were essential for the enhancing the photocatalytic capabilities. The formation of TN/CIS S-scheme by modifying CIS on TN significantly enhanced charge separation. Meanwhile, the CIS as a unique component of S-scheme could facilitate the generation of formic acid to $\cdot CO_2^-$, which was a critical step for the formation of NH_3. And, DFT calculations revealed that the SACu over the SACu/TN/CIS SHPs under illumination further reduced the activation barriers, eventually leading to improved NH_3 production. The rational design of the catalyst led to NH_3 production rate of 256.32 µmol g^{-1} h^{-1} with 88.7 % selectivity. This photocatalytic nitrate synergy

brings the utilization of clean energy one step closer to people's expectations. Our research results are worthy of reference when designing other efficient photocatalysts in the future, especially the synergy can take the conversion efficiency and selectivity into account.

CRediT authorship contribution statement

Zhiyuan Liu: Investigation , Data curation , Methodology, Software, Visualization, Writing – original draft , Visualization. **Shiying Fan:** Methodology, Software, Visualization, Writing – review & editing. **Xinyong Li:** Conceptualization, Formal analysis, Resources, Writing – review & editing, Supervision. **Zhaodong Niu:** Methodology, Software, Visualization, Writing – review & editing. **Jing Wang:** Methodology, Software, Visualization, Writing – review & editing. **Chunpeng Bai:** Methodology, Software, Visualization, Writing – review & editing. **Jun Duan:** Methodology, Software, Visualization, Writing – review & editing. **Moses O. Tadé:** Supervision, Conceptualization, Writing – review & editing. **Shaomin Liu:** Supervision, Conceptualization, Writing – review & editing.

Declaration of Competing Interest

The authors declare that they have no known competing financial interests or personal relationships that could have appeared to influence the work reported in this paper.

Data Availability

The data that has been used is confidential.

Appendix A. Supporting information

Supplementary data associated with this article can be found in the online version at doi:10.1016/j.apcatb.2023.122416.

References

[1] Y. Wang, A. Xu, Z. Wang, L. Huang, J. Li, F. Li, J. Wicks, M. Luo, D. Nam, C. Tan, Y. Ding, J. Wu, Y. Lum, C. Dinh, D. Sinton, G. Zheng, E. Sargent, Enhanced nitrate-to-ammonia activity on copper–nickel alloys via tuning of intermediate adsorption, J. Am. Chem. Soc. 142 (12) (2020) 5702–5708.
[2] M. Jiang, J. Su, X. Song, P. Zhang, M. Zhu, L. Qin, Z. Tie, J. Zuo, Z. Jin, Radial piston triboelectric nanogenerator-enhanced cellulose fiber air filter for self-powered particulate matter removal, Nano Lett. 22 (6) (2022) 2529–2537.
[3] W. Zheng, L. Zhu, Z. Yan, Z. Lin, Z. Lei, Y. Zhang, H. Xu, Z. Dang, C. Wei, C. Feng, Self-activated Ni cathode for electrocatalytic nitrate reduction to ammonia: from fundamentals to scale-up for treatment of industrial wastewater, Environ. Sci. Technol. 55 (19) (2021) 13231–13243.
[4] Y. Wang, W. Zhou, R. Jia, Y. Yu, B. Zhang, Unveiling the activity origin of a copper-based electrocatalyst for selective nitrate reduction to ammonia, Angew. Chem. Int. Ed. 59 (2020) 5350–5354.
[5] Z. Gong, W. Zhong, Z. He, Q. Liu, H. Chen, D. Zhou, N. Zhang, X. Kang, Y. Chen, Regulating surface oxygen species on copper (I) oxides via plasma treatment for effective reduction of nitrate to ammonia, Appl. Catal. B: Environ. 305 (2022), 121021.
[6] X. Zhao, Z. Zhu, Y. He, H. Zhang, X. Zhou, W. Hu, M. Li, S. Zhang, Y. Dong, X. Hu, A. Kuklin, G. Baryshnikov, H. Ågren, G. Hu, Simultaneous anchoring of Ni nanoparticles and single-atom Ni on BCN matrix promotes efficient conversion of nitrate in water into high-value-added ammonia, Chem. Eng. J. 433 (2022), 133190.

[7] Z. Deng, J. Liang, Q. Liu, C. Ma, L. Xie, L. Yue, Y. Ren, T. Li, Y. Luo, N. Li, B. Tang, A. Alshehri, I. Shakir, P. Agboola, S. Yan, B. Zheng, J. Du, Q. Kong, X. Sun, High-efficiency ammonia electrosynthesis on self-supported Co₂AlO₄ nanoarray in neutral media by selective reduction of nitrate, Chem. Eng. J. 435 (2022), 135104.

[8] S. Pan, J. Li, Z. Wen, R. Lu, Q. Zhang, H. Jin, L. Zhang, Y. Chen, S. Wang, Halide perovskite materials for photo(electro)chemical applications: dimensionality, heterojunction, and performance, Adv. Energy Mater. (2021) 2004002.

[9] Z. Liu, L. Wang, X. Yu, J. Zhang, R. Yang, X. Zhang, Y. Ji, M. Wu, L. Deng, L. Li, Z. Wang, Piezoelectric-effect-enhanced full-spectrum photoelectrocatalysis in p-n heterojunction, Adv. Funct. Mater. 29 (2019) 1807279.

[10] J. Li, R. Chen, J. Wang, Y. Zhou, G. Yang, F. Dong, Subnanometric alkaline-earth oxide clusters for sustainable nitrate to ammonia photosynthesis, Nat. Commun. 13 (2022) 1098.

[11] W. Liu, X. Li, X. Chu, S. Zuo, B. Gao, C. Yao, Z. Li, Y. Chen, Boosting photocatalytic reduction of nitrate to ammonia enabled by perovskite/biochar nanocomposites with oxygen defects and O-containing functional groups, Chemosphere 294 (2022), 133763.

[12] C. Jiang, H. Wang, Y. Wang, H. Jia, All solid-state Z-scheme CeO₂/ZnIn₂S₄ hybrid for the photocatalytic selective oxidation of aromatic alcohols coupled with hydrogen evolution, Appl. Catal. B: Environ. 277 (2020) 119235.

[13] Y. Chao, J. Zheng, H. Zhang, F. Li, F. Yan, Y. Tan, Z. Zhu, Oxygen-incorporation in Co₂P as a non-noble metal cocatalyst to enhance photocatalysis for reducing water to H₂ under visible light, Chem. Eng. J. 346 (2018) 281–288.

[14] K. Sun, M. Liu, J. Pei, D. Li, C. Ding, K. Wu, H. Jiang, Incorporating transition-metal phosphides into metal-organic frameworks for enhanced photocatalysis, Angew. Chem. Int. Ed. 132 (2020) 22937–22943.

[15] J. Zhang, T. Bai, H. Huang, M. Yu, X. Fan, Z. Chang, X. Bu, Metal-organic-framework-based photocatalysts optimized by spatially separated cocatalysts for overall water splitting, Adv. Mater. 32 (2020) 2004747.

[16] X. Fang, Q. Shang, Y. Wang, L. Jiao, T. Yao, Y. Li, Q. Zhang, Y. Luo, H. Jiang, Single Pt atoms confined into a metal-organic framework for efficient photocatalysis, Adv. Mater. 30 (2018) 1705112.

[17] Y. Li, Q. Wang, X. Hu, Y. Meng, H. She, L. Wang, J. Huang, G. Zhu, Constructing NiFe-metal-organic frameworks from NiFe-layered double hydroxide as a highly efficient cocatalyst for BiVO₄ photoanode PEC water splitting, Chem. Eng. J. 433 (2022), 133592.

[18] Z. Kang, X. Lv, Z. Sun, S. Wang, Y. Zheng, X. Tao, Borate and iron hydroxide co-modified BiVO₄ photoanodes for high-performance photoelectrochemical water oxidation, Chem. Eng. J. 421 (2021), 129819.

[19] C. Liu, H. Luo, Y. Xu, Z. Zhang, Q. Liang, W. Wang, Z. Chen, Synergistic cocatalyst effect of ultra-thin metal-organic framework and Mo-dopant for efficient photoelectrochemical water oxidation on BiVO₄ photoanode, Chem. Eng. J. 384 (2020), 123333.

[20] J. Kim, J. Yoon, T. Kim, Y. Jo, J. Kim, S. Jeong, J. Lee, Heterostructure between WO₃ and metal organic framework-derived BiVO₄ nanoleaves for enhanced photoelectrochemical performances, Chem. Eng. J. 425 (2021), 131496.

[21] H. Go, I. Akio, T. Tsuyoshi, K. Junko N, H. Michikazu, D. Kazunari, Ta₃N₅ as a novel visible light-driven photocatalyst (λ<600 nm), Chem. Lett. 7 (2002) 736–737.

[22] J. Xiao, J. Vequizo, T. Hisatomi, J. Rabeah, M. Nakabayashi, Z. Wang, Q. Xiao, H. Li, Z. Pan, M. Krause, N. Yin, G. Smith, N. Shibata, A. Brückner, A. Yamakata, T. Takata, K. Domen, Simultaneously tuning the defects and surface properties of Ta₃N₅ nanoparticles by Mg-Zr codoping for significantly accelerated photocatalytic H₂ evolution, J. Am. Chem. Soc. 143 (27) (2021) 10059–10064.

[23] S. Li, J. Chen, S. Hu, H. Wang, W. Jiang, X. Chen, Facile construction of novel Bi₂WO₆/Ta₃N₅ Z-scheme heterojunction nanofibers for efficient degradation of harmful pharmaceutical pollutants, Chem. Eng. J. 402 (2020), 126165.

[24] J. Fu, Z. Fan, M. Nakabayashi, H. Ju, N. Pastukhova, Y. Xiao, C. Feng, N. Shibata, K. Domen, Y. Li, Interface engineering of Ta₃N₅ thin film photoanode for highly efficient photoelectrochemical water splitting, Nat. Commun. 13 (2022) 729.

[25] Y. Pihosh, V. Nandal, T. Minegishi, M. Katayama, T. Yamada, K. Seki, M. Sugiyama, K. Domen, Development of a core-shell heterojunction Ta₃N₅-nanorods/BaTaO₂N photoanode for solar water splitting, ACS Energy Lett. 5 (2020) 2492–2497.

[26] Y. Kawase, T. Higashi, M. Katayama, K. Domen, K. Takanabe, Maximizing oxygen evolution performance on a transparent NiFeOₓ/Ta₃N₅ photoelectrode fabricated on an insulator, ACS Appl. Mater. Interfaces 13 (2021) 16317–16325.

[27] J. Fu, F. Wang, Y. Xiao, Y. Yao, C. Feng, L. Chang, C. Jiang, V. Kunzelmann, Z. Wang, A. Govorov, I. Sharp, Y. Li, Identifying performance-limiting deep traps in Ta₃N₅ for solar water splitting, ACS Catal. 10 (2020) 10316–10324.

[28] W. Chun, A. Ishikawa, H. Fujisawa, T. Takata, J. Kondo, M. Hara, M. Kawai, Y. Matsumoto, K. Domen, Conduction and Valence Band Positions of Ta₂O₅, TaON, and Ta₃N₅ by UPS and Electrochemical Methods, J. Phys. Chem. B 107 (2003) 1798–1803.

[29] Q. Xu, L. Zhang, B. Cheng, J. Fan, J. Yu, S-scheme heterojunction photocatalyst, Chem 6 (2020) 1543–1559.

[30] L. Zhang, J. Zhang, H. Yu, J. Yu, Emerging S-scheme photocatalyst, Adv. Mater. 34 (2022) 2107668.

[31] P. Xia, S. Cao, B. Zhu, M. Liu, M. Shi, J. Yu, Y. Zhang, Designing a 0D/2D S-scheme heterojunction over polymeric carbon nitride for visible-light photocatalytic inactivation of bacteria, Angew. Chem. Int. Ed. 59 (2020) 5218–5225.

[32] X. Li, B. Kang, F. Dong, Z. Zhang, X. Luo, L. Han, J. Huang, Z. Feng, Z. Chen, J. Xu, B. Peng, Z. Wang, Enhanced photocatalytic degradation and H₂/H₂O₂ production performance of S-pCN/WO₂.₇₂ S-scheme heterojunction with appropriate surface oxygen vacancies, Nano Energy 81 (2021), 105671.

[33] C. Cheng, B. He, J. Fan, B. Cheng, S. Cao, J. Yu, An Inorganic/Organic S-scheme heterojunction H₂-production photocatalyst and its charge transfer mechanism, Adv. Mater. 33 (2021) 2100317.

[34] L. Wei, M. Adamson, J. Vela, Ni₂P-modified Ta₃N₅ and TaON for photocatalytic nitrate reduction, ChemNanoMat 6 (2020) 1179–1185.

[35] D. Hao, Y. Liu, S. Gao, H. Arandiyan, X. Bai, Q. Kong, W. Wei, P. Shen, B. Ni, Emerging artificial nitrogen cycle processes through novel electrochemical and photochemical synthesis, Inorg. Chem. 46 (2021) 213.

[36] B. Kale, J. Baeg, S. Lee, H. Chang, S. Moon, C. Lee, CdIn₂S₄ nanotubes and "Marigold" nanostructures: a visible-light photocatalyst, Adv. Funct. Mater. 16 (2006) 1349–1354.

[37] C. Ling, X. Ye, J. Zhang, J. Zhang, S. Zhang, S. Meng, X. Fu, S. Chen, Solvothermal synthesis of CdIn₂S₄ photocatalyst for selective photosynthesis of organic aromatic compounds under visible light, Sci. Rep. 7 (2017) 27.

[38] W. Wang, T. Ng, W. Ho, J. Huang, S. Liang, T. An, G. Li, J. Yu, P. Wong, CdIn₂S₄ microsphere as an efficient visible-light-driven photocatalyst for bacterial inactivation: Synthesis, characterizations and photocatalytic inactivation mechanisms, Appl. Catal. B: Environ. 129 (2013) 482–490.

[39] C. Liu, X. Li, J. Li, Y. Zhou, L. Sun, H. Wang, P. Huo, C. Ma, Y. Yan, Fabricated 2D/2D CdIn₂S₄/N-rGO muti-heterostructure photocatalyst for enhanced photocatalytic activity, Carbon 152 (2019) 565–574.

[40] Y. Yu, G. Chen, G. Wang, Z. Lv, Visible-light-driven ZnIn₂S₄/CdIn₂S₄ composite photocatalyst with enhanced performance for photocatalytic H₂ evolution, Int. J. Hydrogen Energy 38 (2013) 1278–1285.

[41] S. Ma, T. Hisatomi, K. Maeda, Y. Moriya, K. Domen, Enhanced water oxidation on Ta₃N₅ photocatalysts by modification with alkaline metal salts, J. Am. Chem. Soc. 134 (49) (2012) 19993.

[42] S. Chen, Y. Qi, Q. Ding, Z. Li, J. Cui, F. Zhang, C. Li, Magnesia interface nanolayer modification of Pt/Ta₃N₅ for promoted photocatalytic hydrogen production under visible light irradiation, J. Catal. 339 (2016) 77.

[43] Z. Peng, J. Jiang, Y. Xiao, H. Xu, W. Zhang, L. Ni, CdIn₂S₄ surface-decorated Ta₃N₅ core-shell heterostructure for improved spatial charge transfer: In-situ growth, synergistic effect and efficient dualfunctional photocatalytic performance, Appl. Surf. Sci. 487 (2019) 1084.

[44] C. Wang, S. Dong, Y. Wang, T. Guo, G. Gao, Z. Lu, B. Pan, Selective removal of nitrate via the synergistic effect of oxygen vacancies and plasmon-induced hot carriers, Chem. Eng. J. 397 (1) (2020), 125435.

[45] Y. Li, T. Takata, D. Cha, K. Takanabe, T. Minegishi, J. Kubota, K. Domen, Vertically aligned Ta₃N₅ nanorod arrays for solar-driven photoelectrochemical water splitting, Adv. Mater. 25 (2013) 125–131.

[46] F. Xu, K. Meng, B. Cheng, S. Wang, J. Xu, J. Yu, Unique S-scheme heterojunctions in self-assembled TiO₂/CsPbBr₃ hybrids for CO₂ photoreduction, Nat. Commun. 11 (2020) 4613.

[47] L. Wang, Z. Chen, X. Ran, H. Tang, D. Cao, A facile synthesis of Cu(II) diethyldithiocarbamate from monovalent copper-cysteamine and disulfiram, Inorg. Chem. Commun. 137 (2022), 109246.

[48] L. Wang, B. Cheng, L. Zhang, J. Yu, In situ irradiated XPS investigation on S-scheme TiO₂@ZnIn₂S₄ photocatalyst for efficient photocatalytic CO₂ reduction, Small 17 (2021) 2103447.

[49] S. Zhang, M. Li, J. Li, Q. Song, X. Liu, High-ammonia selective metal-organic framework-derived Co-doped Fe/Fe₂O₃ catalysts for electrochemical nitrate reduction, Proc. Natl. Acad. Sci. USA 119 (2022) 6.

[50] J. Yuan, Z. Xing, Y. Tang, C. Liu, Tuning the oxidation state of Cu electrodes for selective electrosynthesis of ammonia from nitrate, ACS Appl. Mater. Interfaces 13 (2021) 52469–52478.

[51] P. Gao, Z. Xue, S. Zhang, D. Xu, G. Zhai, Q. Li, J. Chen, X. Li, Schottky barrier-induced surface electric field boosts universal reduction of NOₓ⁻ in water to ammonia, Angew. Chem. Int. Ed. 60 (2021) 20711–20716.

[52] X. Deng, Y. Yang, L. Wang, X. Fu, J. Luo, Metallic Co nanoarray catalyzes selective NH₃ production from electrochemical nitrate reduction at current densities exceeding 2 A cm⁻², Adv. Sci. 8 (2021) 2004523.

[53] L. Li, C. Tang, X. Cui, Y. Zheng, X. Wang, H. Xu, S. Zhang, T. Shao, K. Davey, S. Qiao, Efficient nitrogen fixation to ammonia through integration of plasma oxidation with electrocatalytic reduction, Angew. Chem. Int. Ed. 60 (2021) 14131–14137.

[54] J. Zhang, Q. Li, C. Ouyang, X. Yu, M. Ge, X. Huang, E. Hu, C. Ma, S. Li, R. Xiao, W. Yang, Y. Chu, Y. Liu, H. Yu, X. Yang, X. Huang, L. Chen, H. Li, Trace doping of multiple elements enables stable battery cycling of LiCoO₂ at 4.6 V, Nat. Energy 4 (2019) 594–603.

[55] L. Azancot, V. Blay, R. Blay-Roger, L. Bobadilla, A. Penkova, M. Centeno, J. Odriozola, Evidence of new Ni-O-K catalytic sites with superior stability for methane dry reforming, Appl. Catal. B: Environ. 307 (2022), 121148.

[56] G. Silva, M. Fernandes, E. Ticianelli, Activity and stability of Pt/IrO₂ bifunctional materials as catalysts for the oxygen evolution/reduction reactions, ACS Catal. 8 (2018) 2081–2092.

[57] D. Lee, S. Sun, J. Kwon, H. Park, M. Jang, E. Park, B. Son, Y. Jung, T. Song, U. Paik, Copper nitride nanowires printed Li with stable cycling for Li metal batteries in carbonate electrolytes, Adv. Mater. 32 (2020) 1905573.

[58] L. Lukashuk, N. Yigit, R. Rameshan, E. Kolar, D. Teschner, M. Hävecker, A. Knop-Gericke, R. Schlögl, K. Föttinger, G. Rupprechter, Operando insights into CO oxidation on cobalt oxide catalysts by NAP-XPS, FTIR, and XRD, ACS Catal. 8 (2018) 8630–8641.

[59] H. Yan, X. Qin, Y. Yin, Y. Teng, Z. Jin, C. Jia, Promoted Cu-Fe$_3$O$_4$ catalysts for low-temperature water gas shift reaction: optimization of Cu content, Appl. Catal. B: Environ. 226 (2018) 182–193.

[60] L. Zhang, J. Mao, S. Li, J. Yin, X. Sun, X. Guo, C. Song, J. Zhou, Hydrogenation of levulinic acid into gamma-valerolactone over in situ reduced CuAg bimetallic catalyst: Strategy and mechanism of preventing Cu leaching, Appl. Catal. B: Environ. 232 (2018) 1–10.

[61] S. Xiong, Y. Peng, D. Wang, N. Huang, Q. Zhang, S. Yang, J. Chen, J. Li, The role of the Cu dopant on a Mn$_3$O$_4$ spinel SCR catalyst: Improvement of low-temperature activity and sulfur resistance, Chem. Eng. J. 387 (2020), 124090.